

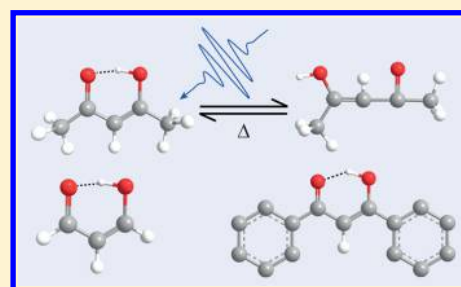
# Ultrafast UV-Induced Photoisomerization of Intramolecularly H-Bonded Symmetric $\beta$ -Diketones

Pramod Kumar Verma, Federico Koch, Andreas Steinbacher, Patrick Nuernberger,<sup>†</sup> and Tobias Brixner\*

Institut für Physikalische und Theoretische Chemie, Universität Würzburg, Am Hubland, 97074 Würzburg, Germany

**S** Supporting Information

**ABSTRACT:** In photoinduced molecular reaction dynamics, the effects of electronic charge redistribution can lead to multiple pathways that are determined by the nature of the initial structures involved and the environment the molecule of interest is studied in. The  $\beta$ -diketones are a common example of this complexity. They show keto–enol tautomerism that is almost totally shifted toward the enolic form. However, compared to the gas phase, the photochemistry proceeds completely differently by virtue of the solvent environment for these compounds, which are used in commercial sunscreen agents due to a high absorption in the ultraviolet (UV) and fast deactivation processes. We disclose these dynamics by investigating three symmetrical  $\beta$ -diketones in various solvents. To observe these effects on an ultrafast time scale directly in the UV spectral region where the relevant electronic transitions take place, we have developed and employed femtosecond transient absorption with detection capability in the deep UV. Our studies confirm that electronic excitation of the chelated enol form does not lead to any ultrafast photochemistry other than proton transfer followed by rotamerization. The formation of the nonchelated conformers takes place on a picosecond time scale through a dark state, whereas the recovery to the stable chelated enol form is a comparably slow process.



## INTRODUCTION

Derivatives of  $\beta$ -diketones are of great importance in diverse research fields by virtue of several remarkable chemical features that lead to a variety of applications.<sup>1</sup> For example, they are widely employed as chelating agents due to their binding affinity for transition metals,<sup>1</sup> or they are even contained in commercial sunscreen products<sup>2–4</sup> owing to the fast deactivation processes after ultraviolet (UV) irradiation. The most prominent property of  $\beta$ -diketones is their keto–enol tautomerism that is shifted almost totally toward the enolic form.<sup>5–7</sup> With structural similarities to relevant biomolecules and photochromic substances on the one hand, and the molecules' own versatility in combination with their structural simplicity on the other hand, small  $\beta$ -diketones are prototypical candidates for a systematic study of the photoinduced processes and the subsequent deactivation channels upon which the wide applicability of  $\beta$ -diketones is based.

Compounds like  $\beta$ -diketones of type  $R-C(O)-CH_2-C(O)-R$ , where  $R = H, CH_3$ , have drawn continuous attention from chemists and physicists of different research areas because of the pronounced keto–enol tautomerism that is observable (and exploitable) in the gas<sup>5,8</sup> and the liquid phase<sup>6,9</sup> and even in isolated cryogenic matrices.<sup>7,10</sup> The reason for the stabilization of the enolic form is an intramolecular H-bond, coupled with a  $\pi$ -electronic delocalization over the  $O-C-C-C-O$  pseudocycle (see Scheme 1). The two simplest and smallest structures exhibiting the central six membered ring closed by the intramolecular H-bond in the chelated enol (CE) form are the compounds malonaldehyde (MA) and acetylacetone (AA; Scheme 1).

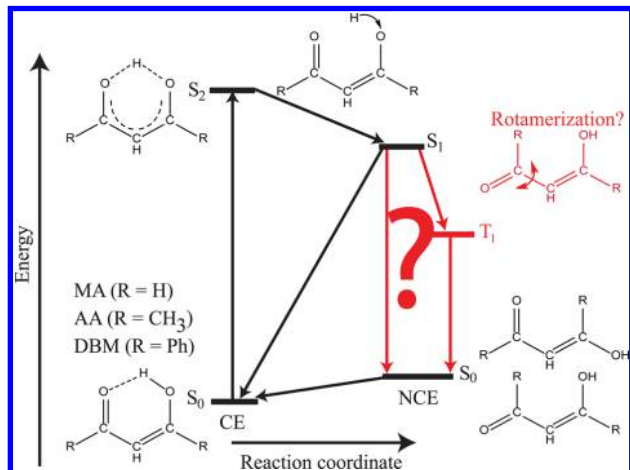
Several nonchelated enol (NCE) rotamers have been identified, i.e., open forms without intramolecular H-bond.<sup>11</sup> They are less stable and rarely observed in liquids.

With regard to the photochemical aspects of  $\beta$ -diketones, various approaches in different phases have been realized both experimentally and theoretically in the literature. It was disclosed that the CE form of  $\beta$ -diketones (Scheme 1) usually exhibits strong absorption bands in the UV originating from the dipole-allowed  $\pi\pi^*$  transitions ( $S_2 \leftarrow S_0$ ), i.e., connecting the ground state with the second excited singlet state.<sup>9</sup> Upon excitation, multiple pathways (tautomerization, isomerization, and fragmentation) are possible and known to be highly sensitive to the environment of the molecule. Without any solvent influences, the reaction sequence proceeds on an ultrafast time scale and several photofragments are generated. Elaborate gas-phase studies<sup>5</sup> showed that the initial relaxation step of enolic AA is the departure from the Franck–Condon region of the  $S_2$  state within approximately 70 fs, followed by a complete transfer from  $S_2$  to  $S_1$  taking roughly 1.4 ps. Subsequently, the rate-limiting step sets in, which is the transfer from  $S_1$  to  $T_1$  by intersystem crossing (ISC) measured to be 250 ps, before dissociation to OH and 3-penten-2-on-4-yl radicals occurs.<sup>8</sup> The scenario upon absorption of UV light is a different one in liquids, where rotamerization is the dominant channel while tautomerization remains limited. Flash photolysis experiments on a number of  $\beta$ -diketones at room temperature<sup>9,12–14</sup> corroborated that UV irradiation breaks the

Received: August 6, 2014

Published: October 9, 2014

**Scheme 1. Energy Diagram of Possible Relaxation Pathways after Photoexcitation of Symmetrical  $\beta$ -Diketones in Solution<sup>a</sup>**



<sup>a</sup>The structure of the initial chelated enol (CE) and the final non-chelated enol (NCE) isomers are presented at the bottom. The NCE conformers either exhibit an *s-trans* arrangement of the  $\alpha,\beta$ -unsaturated keto chromophore that is derived from the CE by rotation around the CO–CH single bond or an *s-cis* arrangement being derived by rotation around the C=C double bond. The initial and final steps of the photochemistry after UV excitation are known,<sup>9,12–14</sup> and corresponding structures are presented in black. The key-step in the isomerization process is the rotation around the C–C or C=C bond in the excited state (colored in red) for which the involved electronic states and connecting pathways are unknown.

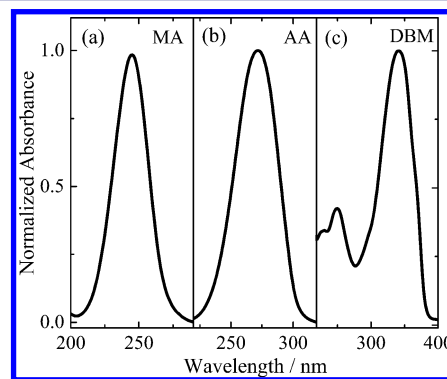
intramolecular H-bond of the CE form, eventually leading to formation of NCE conformers. These structural changes are reversible, since the less stable photoproducts (NCE conformers) convert back to the most stable CE form, to a minor extent to the diketone form or into a mixture of both. This reversibility is a prerequisite, e.g., for an efficient use in sunscreen agents. Moreover, many of the  $\beta$ -diketones are nonfluorescent in solution, suggesting the presence of very efficient (and ultrafast) nonradiative processes from the lowest excited singlet state. Since then, a number of studies have been devoted to isolation and identification of different possible conformers of  $\beta$ -diketones by employing cryogenic matrix isolation experiments<sup>7,10,15</sup> and calculation of their relative energies.<sup>16</sup>

Our study aims to unravel the underlying excited-state processes of  $\beta$ -diketones in the liquid phase and the corresponding time scales and efficiencies. A schematic overview of the involved conformers and associated energy levels is given in Scheme 1. While the initial ultrafast proton transfer in  $S_2$  is widely accepted,<sup>5,8</sup> the subsequent relaxation processes in solution are not disclosed yet (red arrows in Scheme 1), nor are the quantum efficiencies for the formation of NCE species. The formation of the latter requires breakage of the intramolecular H-bond followed by rotamerization around one of the two OC–CH bonds, but given the fast relaxation processes it is decisive from which electronic state the rotamerization takes place. We address this issue by performing time-resolved absorption (TA) experiments on three symmetrical  $\beta$ -diketones, namely malonaldehyde (MA), acetylacetone (AA), and dibenzoylmethane (DBM), which differ only in their terminal substituents (see Scheme 1). By investigating these compounds with different excitation

energies as well as in several solvents, the solvent-dependent quantum efficiencies related to NCE formation are discussed and a coherent picture of the rotamerization dynamics is obtained. Additional picture studies on an acetylacetone-aluminum sec-butoxide (AA–Al) complex, in which the  $\beta$ -diketone acts as a chelating agent and hence the intramolecular H-bond is precluded, complement our detailed study of  $\beta$ -diketone's photoinduced isomerization processes.

## EXPERIMENTAL SECTION

AA (CAS No. 123–54–6) and MA (CAS No. 100683–54–3) were purchased from Sigma-Aldrich; DBM (CAS No. 120–46–7) was obtained from Merck. All the spectroscopic-grade solvents were obtained from Sigma-Aldrich. The steady-state absorption spectra were recorded on a Jasco UV–vis spectrophotometer (model V670) and are shown in Figure 1. AA and DBM were used as received. MA is

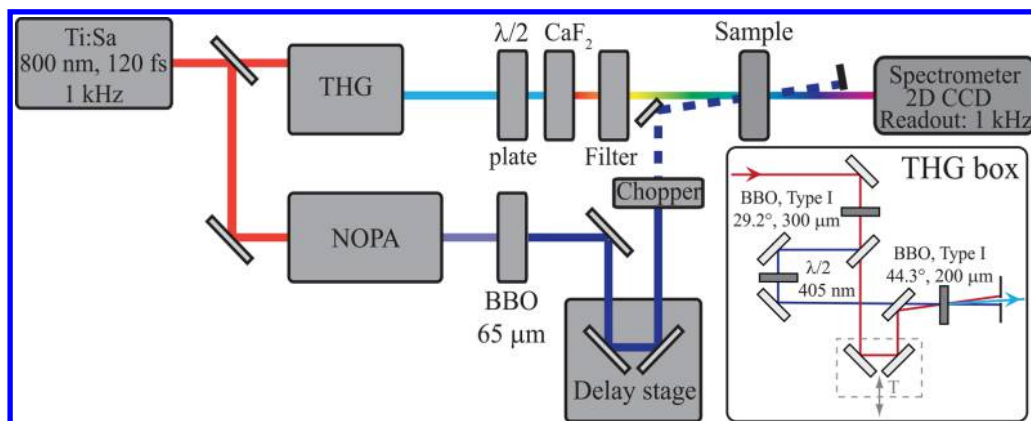


**Figure 1.** Normalized absorption spectra of malonaldehyde (MA) in water at pH 3 (a), acetylacetone (AA) in dioxane (b), and dibenzoylmethane (DBM) in acetonitrile (c).

a reactive compound and hence not commercially available in the pure form. However, its salt form is stable and commercially available. MA was received as tetrabutylammonium salt from Sigma-Aldrich. The salt was dissolved in Milli-Q water and pH was adjusted to 3 (by addition of dilute solution of hydrochloric acid) where the molecule exists as chelated enol form (the absorption peak of the chelated enol form of MA lies close to 245 nm, whereas the deprotonated form, which is dominant at pH 7, absorbs at 267 nm<sup>17,18</sup>). For the transient absorption measurements all samples were prepared to have an absorbance between 0.2 and 0.3 OD (optical density) in the flow cell (sample thickness 200  $\mu$ m) at the respective excitation wavelength.

Since the electronic transitions of  $\beta$ -diketones lie in the UV spectral range (confer the linear absorption spectrum of MA, AA, and DBM in Figure 1), state-of-the-art broadband UV–vis transient absorption experiments that span from 290 to 720 nm<sup>19</sup> are not sufficient. To overcome this limitation, several approaches can be found in the literature, e.g., using UV probe pulses whose center wavelength is tunable,<sup>20</sup> upconverting a visible continuum to the UV,<sup>21</sup> or generating a UV continuum directly with the second<sup>22,23</sup> or third harmonic<sup>22,24</sup> of a Ti:sapphire amplifier. Recent advancement toward this goal has led to some improvement in accessing the UV region down to 230 nm.<sup>25</sup> For the present study, we have implemented femtosecond transient absorption with a continuum probe detection capability in the deep UV ranging from 220 to 330 nm (Scheme 2). This enables us to investigate the excited-state dynamics of the above-mentioned symmetrical  $\beta$ -diketones and opens an avenue for other compounds as well.

The laser system used for the femtosecond transient absorption experiments (Scheme 2) consists of a commercial Ti:sapphire regenerative-amplifier laser system (Spitfire Pro, Spectra-Physics) with output pulses centered at 800 nm with 120 fs duration and 1 kHz repetition rate. A fraction of the output power was used to seed a noncollinear optical parametric amplifier (TOPAS White, Light

Scheme 2. Femtosecond Transient Absorption Setup for Operation in the UV and Visible Spectral Regimes<sup>a</sup>

<sup>a</sup>Layout of the third-harmonic generation (THG) is shown in the inset. After second-harmonic generation in BBO, a HR 400 HT 800 mirror separates 800 and 400 nm beams. Delaying the 800 nm (fundamental) pulse to facilitate overlap and rotating the polarization of the 400 nm pulse to achieve phase matching, the third harmonic is created in another BBO crystal. In the case of visible probing, both BBO crystals are removed and the 800 nm fundamental is focused into CaF<sub>2</sub>.

Conversion Ltd.), which produced the visible pulses (tunable from 500 to 750 nm) that were further frequency doubled in a 65- $\mu\text{m}$   $\beta$ -barium borate (BBO) crystal to generate UV pump pulses (250–375 nm). About 88 mW of the Ti:sapphire output was used to generate 3.9 mW of third harmonic centered at 267 nm (THG box in Scheme 2). Approximately, 300  $\mu\text{W}$  of the 267 nm light was focused into a linearly moving 5 mm thick CaF<sub>2</sub> plate to produce a UV white-light supercontinuum probe ranging from 220 to 330 nm. We used a custom-designed spectral filter (Laser Components GmbH) to suppress the high spectral power of the third harmonic (267 nm) of the fundamental contained within the UV supercontinuum probe.

The supercontinuum probe was focused onto the sample to a spot size of 82  $\mu\text{m}$   $\times$  53  $\mu\text{m}$  by a focusing mirror with focal length of 15 cm. The typical spot size of the pump beam on the sample was 115  $\mu\text{m}$   $\times$  80  $\mu\text{m}$ . The pump and probe pulses were spatially overlapped in noncollinear geometry in a 200  $\mu\text{m}$  flow cell under magic-angle configuration of pump and probe polarization.<sup>26</sup> After passing the sample, the probe pulses were spectrally dispersed and detected via a spectrograph (Acton SP2500i) equipped with a CCD camera (Princeton Instruments Pixis 2k), whereas the pump pulse was blocked. A mechanical chopper, working at 500 Hz, blocked every second pump pulse, thus enabling low-noise shot-to-shot measurements. By comparing the transmitted spectral intensity of consecutive probe pulses [ $I_{\text{pumped}}(\lambda, t)$ ,  $I_{\text{unpumped}}(\lambda)$ ] the photoinduced change in the absorbance was directly recorded as  $\Delta\text{Abs} = -\log[(I_{\text{pumped}}(\lambda, t)/I_{\text{unpumped}}(\lambda))]$ . The time delay  $t$  between pump and probe pulses was varied by allowing the pump pulse to pass through an optical delay line as shown in Scheme 2. When visible continuum was required, the fundamental 800 nm beam, rather than the third harmonic, of the amplifier system was focused into CaF<sub>2</sub>. This was achieved by removing BBO crystals inside the THG box and replacing some of the mirrors with 800 nm high reflector mirrors.

The contribution to the transient absorption signal arising purely from the solvents in the UV and visible regions was checked by recording transient absorption data in a cuvette with neat solvents. The pump-induced changes in absorbance arising purely from solvents were found to be negligible when compared to the signal from  $\beta$ -diketones as shown in Figure S1 of the Supporting Information. We made sure that the effects of varying pump–probe overlap for longer delay times due to misalignment or changes in the divergence of the pump beam, which in general would cause a continuous loss of signal regardless of its sign or spectral position, was not observed during measurement.

Data analysis of the transient map consisting of a three-dimensional data set (wavelength, delay time  $t$ , and  $\Delta\text{Abs}$ ) was performed with the global and target analysis program Glotaran based on the statistical fitting package TIMP.<sup>27–29</sup> During the fitting procedure, the

parameters for instrument-response function, dispersion, and coherent artifact were included in the model as per the availability in the Glotaran software. The results of the fitting are either presented in the time domain by plotting transients and associated fits, i.e., a cut along the time delay  $t$ , or in the wavelength domain. In the second case, depending on the global fitting model either evolution-associated spectra (EAS) or decay-associated spectra (DAS) are presented. For the latter a parallel model<sup>30</sup> is assumed and every spectrum corresponds to the wavelength-dependent amplitudes of one exponential decay component. In the case of a sequential model<sup>30</sup> every EAS corresponds again to one exponential decay that now also constitutes the population for the subsequent decay. Finally, the result of a target analysis, which is often described by a compartment model, can be presented with species-associated spectra (SAS) each of which belongs to one species (compartment) that may be populated and depopulated by several, possibly bifurcating paths.

## RESULTS AND DISCUSSION

To obtain a conclusive picture of the primary photoprocesses that set in after absorption of UV radiation in  $\beta$ -diketones, we start our comparative study with the transient absorption (TA) spectra of AA recorded for delay times up to 3.2 ns. In the transient map of AA excited at 265 nm in Figure 2, three distinct features can be observed. One is the bleach of ground state (GSB) population that results in the negative signal around 250–300 nm (blue). The second feature is a positive signal (yellow/red) at early delay times, corresponding to excited-state absorption (ESA) from the excited species. A third feature at later delay times, which is also positive, can either be attributed to a slow triplet relaxation pathway or the formation of a photoproduct. The kinetic traces of four selected wavelengths of the transient map are shown in Figure 3. The transient at 283 nm (gray) describes solely the evolution of the GSB. Following the progression of this transient over time it becomes clear that several time constants are involved. Hence, there are multiple relaxation steps to repopulate the ground state of AA after UV excitation. As already visible from the TA map (Figure 2) and also observable in the transient for 241 nm (red), the ESA and GSB contributions overlap. Five time constants were needed to fit AA's relaxation dynamics as shown in Table 1 (a comparison of fitting quality with 5 versus 4 time components in global fitting is shown in Figure S2 of the

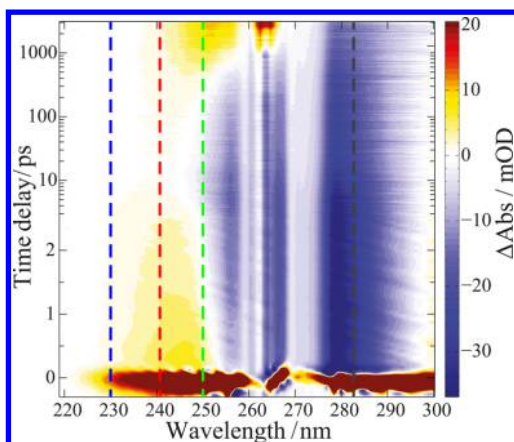


**Figure 2.** Transient absorption map of acetylacetone (AA) in dioxane after excitation with 265 nm. The “uneven”  $\Delta$ Abs between 260 and 275 nm is due to the characteristic of the filter used for suppressing the intensity of the third harmonic of the Ti:sapphire output that in turn also reduces the supercontinuum probe intensity. Note that the vertical axis is plotted on a linear scale up to 2 ps and then on a logarithmic scale. The kinetic traces at selected wavelengths (dashed lines) are shown in Figure 3

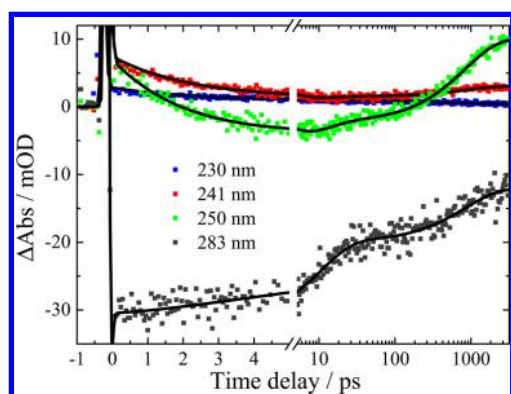


**Figure 3.** Kinetic traces at four selected wavelengths (vertical dashed lines in Figure 2) reflecting the ultrafast dynamics of acetylacetone (AA). Fit results from the global fitting routine are shown in black. Note that the abscissa is plotted on a linear scale up to 5 ps and then on a logarithmic scale.

**Table 1. Time Components and Product-Formation Efficiency Obtained by Global Analysis for the Ultrafast Photodynamics of AA Excited with Different Excitation Energies**

$\beta$ -diketone (solvent)	excitation (nm)	$\tau_1^a$ (fs)	$\tau_2$ (ps)	$\tau_3$ (ps)	$\tau_4$ (ns)	$\tau_5^b$ (ns)	NCE product (%)
AA (dioxane)	248	50	1.96	18.3	1.13	10	27
AA (dioxane)	265	50	2.25	9.80	0.84	10	29
AA (dioxane)	285	50	1.43	6.02	0.75	10	28

<sup>a</sup>The 50 fs component is an upper limit that is below the instrumental time resolution. <sup>b</sup>The fifth time component ( $\tau_5$ ) is fixed to 10 ns during the global fitting due to the presence of an offset in the transient map.

Supporting Information). The corresponding EAS and DAS are shown in Figure S3 of the Supporting Information.

The electronic excitation of AA with 265 nm populates the first bright state  $S_2$  (bright state because of the dipole-allowed  $\pi\pi^*$  transition), initiating an ultrafast departure from the Franck–Condon region that can be tracked by observing ESA dynamics. An upper limit of  $\tau_1 \approx 50$  fs could be derived for the time constant of the primary reaction process, which however is faster than our time resolution determined by the laser cross correlation. This ultrafast initial step might correspond to a change of molecular structure, e.g., the proton transfer from one oxygen atom toward the other as indicated in Scheme 1. In the ground state AA exhibits an asymmetric ( $C_s$ ) structure (where the central H atom belongs to only one oxygen atom), and hence the geometry of the AA in the Franck–Condon region corresponds to an asymmetric structure where the H atom is closer to one of the oxygen atoms.<sup>31</sup> However, after the excitation, this asymmetry is broken as indicated by experimental and theoretical studies,<sup>5,32–36</sup> leading to a pseudoaromaticity. The 50 fs limit is very similar to the proton transfer rates of many related systems, e.g., *o*-hydroxybenzaldehyde, 1-hydroxy-2-acetonaphthone, methyl salicylate, 2-(2'-hydroxyphenyl)benzoxazole, and TINUVIN P.<sup>37–40</sup>

With the time scale of  $\tau_2 = 2.25$  ps, the decrease of the ESA feature in the spectral range from 230 to 250 nm can be observed in the presented transients at 230 and 241 nm (confer Figure 3). This time constant is in agreement with ultrafast studies of AA in the gas phase<sup>5,8</sup> where the time scale of  $\approx 1.4$  ps was assigned to the dynamics in the region of strong coupling between  $S_2$  ( $\pi\pi^*$ ) and  $S_1$  ( $n\pi^*$ ), presumably a conical intersection, close to the equilibrium geometry of the  $S_2$  surface. Furthermore, the absorption spectrum of the enolic AA in a supersonic jet, deduced from the OH photofragment excitation spectrum, shows no distinct structures suggesting the very fast nonradiative decay of the excited state.<sup>41</sup> These observations can explain the fact that AA is nonfluorescent since the  $S_2$  lifetime is so short and the  $S_1$  state is spectroscopically dark. The transient at 250 nm reaches negative values, due to the overlapping of GSB and the diminishing ESA. Furthermore, the evolution-associated spectra (EAS, see Figure S3b of the Supporting Information) for  $\tau_2$  evidence a loss of amplitude in the positive ESA band around 245 nm, whereas the amplitude remains unchanged at the ground state bleaching band of 280 nm. This shows an ultrafast relaxation from the  $S_2$  ( $\pi\pi^*$ ) to the next accessible excited state, which can be assigned to the  $S_1$  ( $n\pi^*$ ) state.<sup>5,8,34</sup>

The GSB amplitude of the transients at 250 and 283 nm decreases afterward on the  $\tau_3 = 9.80$  ps time scale. The same feature can be observed in the EAS (Figure S3b) and corroborates that the excited AA molecules partly relax back to their ground state. With  $\tau_4 = 0.84$  ns the GSB amplitude decreases further (gray transient at 283 nm in Figure 3), while the transients at 250 nm (green) and 241 nm (red) clearly rise to a positive OD value.

To clarify the origin of the positive feature around 250 nm for long delay times we also performed TA experiments with the probe tuned to the visible spectral range. The results are presented in Figure S4 of the Supporting Information. As no indication for a triplet relaxation pathway could be observed (e.g., triplet–triplet absorption) this positive feature can be assigned to a photoproduct, namely the NCE form of AA (see Scheme 1). The resulting absorption spectrum of this photoproduct (Figure 4) is in good agreement with the absorbance spectra of the two NCE forms of AA as observed in cryogenic matrix isolation experiments.<sup>11,42</sup> Because of this

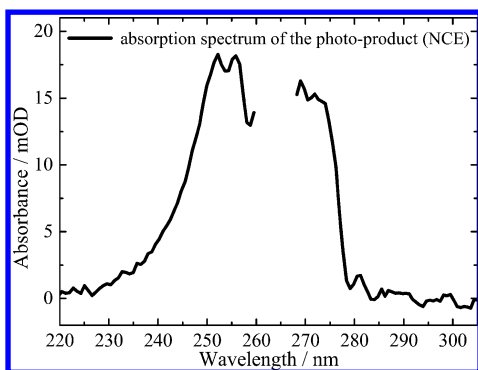


**Figure 4.** Reconstructed absorption spectrum of the photoproduct of AA excited at 265 nm observed after 3074 ps (also see the Figure S5 of the Supporting Information for its detailed reconstruction). Data between 260 and 267 nm was cut out to remove pump-scattering contributions.

finding, we connect the time constant  $\tau_3$  to the depopulation of the  $S_1$  state, which comprises both a contribution of  $S_0$  repopulation and the formation of the NCE photoproducts. This is reasonable since experimental and quantum-chemical studies of  $\beta$ -diketones<sup>12,14,32–34</sup> have shown that the molecule must rearrange (rotamerization) in the first excited state  $S_1$  before the final photoproducts are formed.

As the rotamerization within  $\tau_3$  is the key process in the NCE formation of AA we further investigate the evolution toward the photoproduct in more detail by varying the excess energy, by varying the solvent surrounding AA, by coordinating AA's chelate (O–C–C–C–O) group to Al, and by exchanging the terminal substituents of the symmetric  $\beta$ -diketone.

First, we performed the TA measurements in the same solvent, dioxane, but shifting the pump wavelength from 265 to 248 and 285 nm to observe the influence of excess energy in product formation. The time components obtained through global fitting of the respective transient spectra are also summarized in Table 1. The relaxation from the excited  $S_2$  to the  $S_1$  state, related to the time constants  $\tau_1$  and  $\tau_2$ , remains almost unaltered as compared to 265 nm excitation. A distinct trend can be observed for  $\tau_3$  and  $\tau_4$ , which display a slower relaxation with higher excitation energy. This can be seen in the kinetic traces of GSB recovery (see the kinetic traces at 281 nm in Figure S6 of the Supporting Information) where in case of 248 nm excitation the repopulation of the ground state is slower compared to the transients with excitation wavelength tuned to 265 and 285 nm. Ab-initio molecular dynamic simulation on MA has revealed that there are two pathways from the initially populated  $S_2$  state, one being in-plane evolution followed by reversible proton exchange and finally populating the  $S_1$  state through a nearby  $S_2/S_1$  conical intersection.<sup>35</sup> The second path includes a torsion about the C=C bond that opens up the chelate ring providing efficient quenching to both  $S_1$  and  $S_0$ . A balance between these two

pathways is expected to influence the repopulation of  $S_0$ . Considering the same situation prevails for AA, the excess energy put during the excitation might favor one path over the other as reflected in the observed time constants  $\tau_3$ . However, our data reveals that no additional pathways are found to the photochemistry of AA in the liquid phase. This is in contrast to the cryogenic matrices experiments where AA in parahydrogen solids upon continuous irradiation at 248 nm forms the keto form, though in a very small amount compared to the formation of the NCE form.<sup>43</sup> Hence, for all three pump wavelengths the formation of the NCE form through rotamerization as suggested above, takes place predominantly within the first nanoseconds. The percentage of photoproduct formation of AA in dioxane has been derived for the three different excitation wavelengths and was found to be 27, 29, and 28% upon excitation at 248, 265, and 285 nm, respectively (see Table 1). The percentage of the photoproduct formed was calculated by dividing the  $\Delta$ Abs value of the photoproduct (at the peak position of 252 nm and at the longest delay times) with the  $\Delta$ Abs value of the initial ground-state bleach (at the peak position of 279 nm). This approach is reasonable since the extinction coefficients of the CE and NCE form are comparable.<sup>9</sup> However, as the dynamics of the formation of the photoproduct are supposedly not completed in the experimentally accessible time window the uncertainty in the NCE product percentages is larger than the difference found for different excitation wavelengths. Note that before the division, the value of  $\Delta$ Abs was averaged over 10 delay times for both initial bleach signal (first 10 steps of delay following the temporal pump–probe overlap) and final photoproduct signal (last 10 steps of delay). Although the relaxation rates show a dependence on the excess energy, the product formation yield is not influenced and yields similar amounts of the NCE photoproduct. Therefore, the excess energy does not lead to a different reaction outcome, as would for instance be possible by accessing higher-lying states from which the reaction proceeds differently<sup>44,45</sup> or by an altered branching due to wave packet splitting on the excited-state surface.<sup>46,47</sup>

Having disclosed that the amount of product is independent of the excitation energy, we performed additional TA measurements of AA in the nonpolar solvent *n*-hexane and the polar aprotic solvent acetonitrile to understand the influence of the molecular environment. The kinetic time components of the fit for AA in acetonitrile and *n*-hexane are summarized in Table 2. The increase in solvent polarity decreases the percentage of CE from 95% (in *n*-hexane) to 82% (in dioxane) and further to 62% in acetonitrile,<sup>48</sup> however the absorption peak position among all solvents remains almost the same (only its magnitude varies). The percentages of photoproduct formed in these three solvents are found to be 15% (*n*-hexane), 29% (dioxane), and 36% (acetonitrile). This clear trend can be understood by solvent polarity ( $\pi^*$ ) and specific solute–solvent interaction, especially the H-bond-

**Table 2. Time Components Obtained by Global Analysis for the Ultrafast Photodynamics of AA in Different Solvents**

$\beta$ -diketone (solvent)	excitation (nm)	$\tau_1^a$ (fs)	$\tau_2$ (ps)	$\tau_3$ (ps)	$\tau_4$ (ns)	$\tau_5^b$ (ns)	NCE product (%)
AA (dioxane)	265	50	2.25	9.80	0.84	10	29
AA (acetonitrile)	265	50	2.13	–	0.79	10	36
AA ( <i>n</i> -hexane)	265	50	2.12	–	0.82	10	15

<sup>a</sup>The 50 fs component is an upper limit that is below the instrumental time resolution. <sup>b</sup>The fifth time component ( $\tau_5$ ) is fixed to 10 ns during the global fitting due to the presence of an offset in the transient map.

accepting capability ( $\pi^* = 0.55$  and  $0.75$  for dioxane and acetonitrile, respectively).<sup>49</sup> Thus, the NCE photoproduct formation of AA cannot be influenced by excess energy in the excited  $S_2$  state but it can be influenced by the right choice of solvent.

Up to now, all results corroborate that the rotamerization toward NCE takes place within a few picoseconds after photoexcitation and is the key step in the relaxation dynamics for the formation of the photoproducts. However, symmetrical  $\beta$ -diketones are also utilized as chelating agents where the two oxygen atoms coordinate to a metal so that both ultrafast proton transfer and rotamerization are hindered and no corresponding product absorption should occur. Hence, we also investigated the acetylacetonate-aluminum *sec*-butoxide complex (AA-Al). The AA-Al complex has an absorption band at 283 nm that is shifted by 13 nm with respect to that of the  $\pi\pi^*$  transition of the enol form of AA<sup>50</sup> (see Figure S7 of the Supporting Information). This red shift reflects the chemical interaction between AA and Al. The transient spectra at different delay times of the AA-Al complex and AA in aqueous solution are presented in Figure 5. There is only GSB

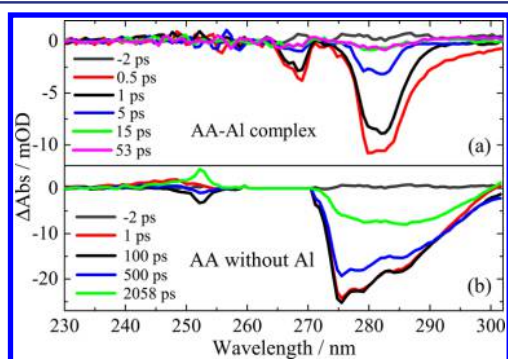


**Figure 5.** Difference spectra of AA-Al complex (a) and AA without Al (b) at different delay times after 270 nm excitation (close to the respective absorption maxima). The “uneven”  $\Delta$ Abs between 260 and 275 nm is due to the characteristic of the filter used for suppressing the intensity of the third harmonic of the Ti:sapphire output that in turn also reduces the supercontinuum probe intensity. In panel (b) the  $\Delta$ Abs values between 260 and 270 nm are set to zero as a result of removing the pump-scattering contributions.

recovery observed in the case of the AA-Al complex (Figure 5a). This recovery is complete within 10 ps and at later delay times no signal is present at all, showing the absence of triplet pathways or photoproduct formation. The observation of this fast deactivation is supported by dielectric relaxation studies of tetrahedral, octahedral, and cubic complexes of AA, in which relaxation times of 4–5 ps were derived,<sup>51</sup> connected most probably to an intramolecular relaxation process involving highly damped oscillations of the chelate rings relative to the remainder of the molecule.<sup>51</sup> On the other hand, the formation of a photoproduct can be clearly observed at long time delay in the case of pure AA in solution (green curve in Figure 5b) from the positive feature around 252 nm. Comparing both data sets of Figure 5 directly reveals that the disruption of the intramolecular H-bond of the chelated enol conformer by chemical modification inhibits the photoproduct formation. Thus, isomerization of AA may be increased by the right choice of solvent, but evidently the product formation can also be inhibited by the disruption of the intramolecular H-bond of the chelated enol conformer by chemical modification.

Another way of chemical modification is to exchange the terminal substituents (R) of symmetric  $\beta$ -diketones ( $R-C(O)-CH_2-C(O)-R$ ). Hence, the photoinduced isomerization process of the symmetric  $\beta$ -diketones MA (R = H) and DBM (R = Ph) that share a common chelate ring similar to AA (R = Me) have also been studied and compared. The absorption spectrum of the simplest  $\beta$ -diketone, MA, is shown in Figure 1a. Its absorption band at 245 nm, which is blue-shifted compared to both AA and DBM, can be attributed to the  $\pi\pi^*$  transition of the chelated enol form. This behavior originates from the change in the strength of intramolecular H-bonding that increases from MA ( $\approx 12$  kcal mol<sup>-1</sup>) to DBM (19 kcal mol<sup>-1</sup>).<sup>52</sup> We measured the transient absorption spectrum of MA in aqueous solution of pH 3. In the transient spectrum, we observe GSB and product absorption (Figure 6a).

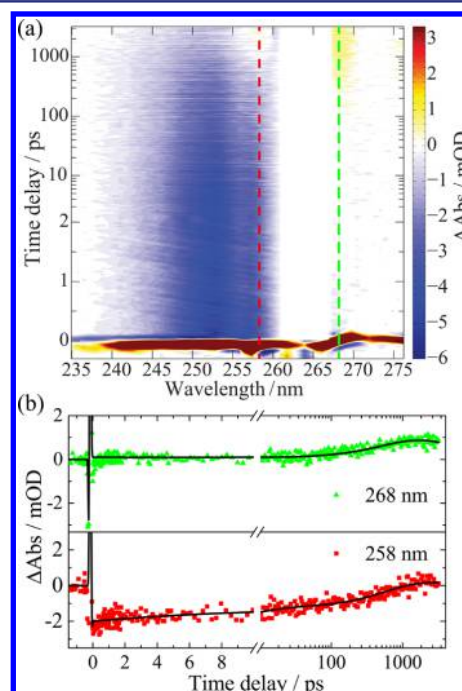


**Figure 6.** (a) Transient absorption map of malonaldehyde (MA) at pH 3 after excitation with 263 nm. The missing  $\Delta$ Abs data between 261 and 266 nm is to remove the pump scattering. The filter used to suppress the third harmonic of Ti:sapphire also reduces the supercontinuum intensity between 260 to 275 nm. Note that the time-delay axis is plotted on a linear scale up to 2 ps and then on a logarithmic scale. (b) Kinetic traces at two selected wavelengths (vertical dashed lines in transient map) of MA. Fit results from the global fitting routine are shown in black. Note that the abscissa is plotted on a linear scale up to 10 ps and then on a logarithmic scale.

In contrast to AA, we do not observe any ESA in the transient map for MA. This could be due to ESA signals that have negligible intensities or that are located even below 220 nm where we do not probe with the broadband UV white-light. Nevertheless, photoproduct absorption starts growing after  $\approx 200$  ps (see the kinetic traces at 258 and 268 nm in Figure 6b) and can be attributed to one of the NCE conformers formed upon UV irradiation. This absorption band ranging from 255 to 271 nm (as seen in the transient map of MA in Figure 6a) is in good agreement with the absorption spectrum of the nonchelated *s-trans* enol form of MA in ref 18.

Compared to MA and AA, the first absorption band ( $\pi\pi^*$ ) in DBM is further shifted to lower energy ( $\approx 330$  nm, Figure 1c)

due to extended conjugation by presence of electron-rich phenyl groups. The second peak at 250 nm in DBM includes a contribution from the small content of the diketone form.<sup>53</sup> The transient absorption measurements of DBM (excitation wavelength 340 nm) both in the UV (Figure 7) and the visible

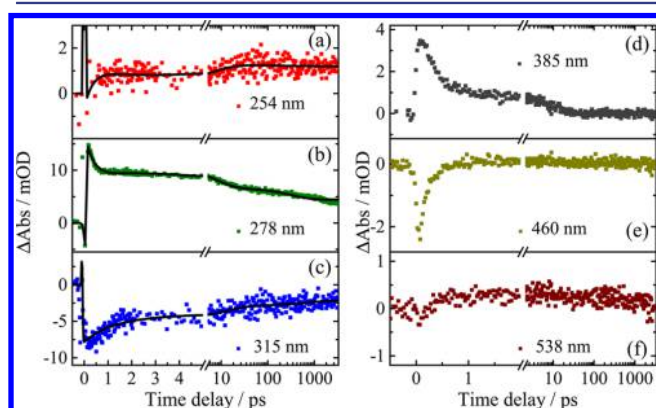


**Figure 7.** Kinetic traces of dibenzoylmethane (DBM) in acetonitrile at six different wavelengths covering the UV (a, b, c and d) and the visible region (e and f), extracted from the full transient maps. Fit results from the global fitting routine are shown in red (a, b and c). Note that the abscissa is plotted on a linear scale up to 5 ps in a, b and c and up to 2 ps in d, e and f and then on a logarithmic scale.

region (Figure S8 of the Supporting Information) have been performed in acetonitrile. The ESA in DBM is very broad and is present in both the UV and the visible region of the TA map. In line with AA, the ESA decays on an ultrafast time scale (147 fs) that is attributed to the primary proton transfer process in the  $S_2$  state. This time scale is very close to excited-state intramolecular proton transfer (ESIPT) in an unsymmetrically substituted 1,3-diketone (*N,N*-dimethylanilino-1,3-diketone).<sup>54</sup> The absorption signal in the deep UV (see the kinetic trace at 278 nm in Figure 7b) remains present up to 3.2 ns, whereas the ESA in the near UV and visible (see the kinetic trace at 385 nm in Figure 7d) decays completely within 14 ps. This difference can be attributed to two reasons. First, the near UV and visible probe photons having less energy compared to deep UV photons cannot promote the molecule to higher electronically excited levels after initial relaxation. Second, the photoproduct formed upon UV irradiation of DBM through isomerization also has an absorption peak near 260 nm,<sup>9,12</sup> which has been confirmed through flash photolysis experiments. The remaining ESA signal in the UV region is probably due to an overlap of the decaying ESA component and the growing positive signal from product absorption. A closer look at the transient data reveals a growing positive signal on a hundred of picoseconds time scale (see the kinetic trace at 254 nm in Figure 7a) that corroborates formation of the NCE conformers on a time scale similar to the other  $\beta$ -diketones studied here. In contrast to the TA data of AA and MA, ultrafast stimulated emission (420–

520 nm; see the transient map in Figure S8 of the Supporting Information) can be induced in DBM. Though DBM does not show any fluorescence (emission maximum at 425 nm) at 77 K<sup>53</sup> that confirms the simulated emission (SE) assignment in the ultrafast experiments. The presence of electron-rich benzene rings on both sides of the chelate ring in DBM reduces the energy gap between the  $S_2$  and  $S_1$  state due to extended conjugation. This should explain the SE, which is a common feature of  $\beta$ -diketones if the excited  $\pi\pi^*$  state has a lower energy than the  $n\pi^*$  state, e.g., 1-hydroxy-2-acetonaphthone and *N,N*-dimethylanilino-1,3-diketone.<sup>37,54</sup> The growing ESA on a time scale of few ps in the visible region (kinetic trace at 538 nm in Figure 7f), can be related to the fact that there is a weak ISC contribution from the singlet state to a triplet state (which should absorb in the visible region). This ISC to the triplet state is believed to be responsible for the formation of the keto form and irreversible photodegradation of DBM;<sup>13</sup> i.e., the pathway via the triplet in Figure 1c is possible for larger  $\beta$ -diketones in solution.

From these comparative studies, we find that the efficiency for NCE product formation is smaller for MA and DBM and larger for AA (see Table 3). As discussed earlier there are two primary decay channels immediately after photoexcitation to the  $S_2$  state; one in-plane evolution leading to ultrafast reversible proton transfer and the other being torsion about the C=C bond. These channels appear to be very efficient for the smallest  $\beta$ -diketone, MA.<sup>35</sup> It is also to be noted that the GSB recovery of MA is almost complete within the experimental time window (see Figure 6) compared to AA and DBM. With the increase in the mass of the substituents in larger  $\beta$ -diketones, the kinetics may tip to favor a greater percentage of ESIPT prior to twisting (if such motion is available at all), which appears to be the case for AA and DBM. However, in case of DBM, the reordering of the excited states as discussed above due to presence of electron-rich and bulky phenyl groups opens up other channels, like SE and ISC, which in turn affects the rotamerization and hence formation of photoproducts.

The performed experiments elucidate the excited-state photochemistry of AA and its dependence on solvent along with the effect of substituents. Furthermore, our data confirms that the relaxation of AA (CE form) in organic solvents after UV irradiation includes an ultrafast relaxation from the  $S_2$  to the  $S_1$  state. From the  $S_1$  state it has been suggested that the molecule may further relax directly to the ground state and stay in the CE form or undergo rotamerization leading to the NCE photoproduct.<sup>9,12,14,34,55</sup> In order to quantify the contributions of these competing reaction pathways, we have performed a target analysis of the TA data with various different target models. In the target model yielding the highest accuracy with the data, the bifurcations from the  $S_1$  state are implemented by assuming that the molecule in the first electronic excited state

**Table 3. Time Components Obtained by Global Analysis for the Ultrafast Photodynamics of Different Symmetric  $\beta$ -Diketones**

$\beta$ -diketone (solvent)	excitation (nm)	$\tau_1^a$ (fs)	$\tau_2$ (ps)	$\tau_3$ (ps)	$\tau_4$ (ns)	$\tau_5^b$ (ns)	NCE product (%)
AA (acetonitrile)	265	50	2.13	–	0.79	10	36
MA (pH 3)	263	–	–	9.07	0.59	10	17
DBM (acetonitrile)	340	147	1.18	10.75	0.49	10	23–30

<sup>a</sup>The 50 fs component is an upper limit that is below the instrumental time resolution. <sup>b</sup>The fifth time component ( $\tau_5$ ) is fixed to 10 ns during the global fitting due to presence of an offset in the transient map.

can exist initially in a conformation that is close to the CE geometry, and then can twist to a partially rotated intermediate that is the precursor of the NCE photoproduct. From both states it can relax back to the CE ground state but only from the NCE precursor it is possible to form the NCE photoproduct. The pictorial representation of our model is shown in Scheme S1 and the corresponding SAS are presented in Figure S9 of the Supporting Information. The target analysis yields corresponding time constants of 7.12 ps for the rotamerization in  $S_1$  and 0.82 ns for the final photoproduct formation, respectively. From the derived branching ratios of 9:91 and 6:94 (for details see Scheme S1 and Figure S9 of the Supporting Information) and also from the kinetic trace of AA at 283 nm in Figure 3, one can infer that there are indeed several origins for  $S_0$  repopulation. It should be noted that a decreasing bleach signal could in principle be due to either  $S_0$  repopulation or an evolving ESA or photoproduct absorption spectrally overlapping with the bleach signal. In the case of the  $\beta$ -diketones studied here the  $S_0$  repopulation is further corroborated by the theoretical prediction of a direct recovery pathway.

The ultrafast nonradiative relaxation to the ground state along with the rotamerization process in the excited state leading back to the original photoexcited conformer (on time scales much longer than observable in our experiments) evidence that  $\beta$ -diketones and derivatives are suitable compounds for UVA sunscreen agents<sup>2,3</sup> as once in the ground state, these molecules can absorb another photon to repeat the nonradiative process, thereby effectively shielding the skin from damage by UV radiation. The variation of solvent, substituents, and the excess energy provided a comprehensive picture of the photoinduced process and formation of NCE photoproducts that necessitates a rotamerization in the electronic excited state. While the product formation is mostly independent of excess energy, it strongly depends on the solvent and chemical modification, e.g., coordination to a metal or substitution of the residual groups of the symmetric  $\beta$ -diketone. These influences may lead to an increasing product formation or even prevent it completely. Besides photoproduct formation, also efficient direct relaxation pathways back to the ground state could be identified, again underlining the suitability of  $\beta$ -diketone derivatives for sunscreen agents.

## CONCLUSIONS

Comparing the ultrafast photochemistry of three structurally similar  $\beta$ -diketones that share a common chelate ring, we find a distinct photoproduct formation on a hundreds-of-picoseconds time scale. The primary photoinduced processes, proton transfer, internal conversion, rotamerization followed by the formation of the NCE photoproduct, have been explored and discussed in detail for AA and were compared to those of MA and DBM. This has been possible by developing and employing an advanced femtosecond pump–probe setup with unprecedented continuum probing down to 220 nm. The transient absorption measurements reveal ultrafast proton transfer on a time scale of less than 50 fs for AA. This is followed by population transfer from the initially bright state ( $^1\pi\pi^*$ ,  $S_2$ ) to a dark state ( $^1n\pi^*$ ,  $S_1$ ) occurring within a few picoseconds, and subsequent rotamerization proceeds on a time scale of about 10 picoseconds in the  $S_1$  excited state. This is followed by formation of nonchelated enol (NCE) conformers on a subnanosecond time scale that then revert back to the most stable chelated conformer (CE) on time scales inaccessible to our technique. Besides this rotamerization, also direct relaxation

from the  $S_1$  state to the initial CE conformer ground state has been disclosed. The compounds exhibit predominantly non-radiative dynamics and show remarkable stability against degradation caused by UV radiation, confirming their wide applicability as sunscreen agents.

Our study rules out the additional relaxation pathway particularly due to laser-induced formation of the diketone from the CE form of  $\beta$ -diketones on an ultrafast time scale. Furthermore, the absorbance band of the photoproduct (NCE conformer) of MA has been identified in the present study, which is formed on a time scale of roughly 200 ps and is red-shifted with respect to the absorption of the reactant. This shift is in contrast to  $\beta$ -diketones with larger substituents, like AA and DBM. Substitution of the methyl groups of AA with electron-rich aromatic rings leads to the appearance of additional processes, e.g., stimulated emission and intersystem crossing. The differences in the ultrafast photochemistry of the three compounds are attributed to the possibility of extended conjugation and the bulky nature of the phenyl ring in DBM as compared to the smaller molecules AA and MA. In solvent-dependent measurements of the photochemistry of AA, the stabilizing nature of specific solute–solvent interactions and their influence on the photoproduct yield has been elucidated. We would like to point out that although there are numerous theoretical studies of  $\beta$ -diketone and its photochemistry,<sup>10,32,34,35,56,57</sup> it would be beneficial to investigate the ultrafast photochemistry of  $\beta$ -diketones including solvent effects with state-of-the-art computational methods. These could provide very valuable additional insight into the molecules' potential energy surfaces and the associated dynamics with solvent influences taken into account. The analysis of the ultrafast experimental data presented here already provides a lucid overall picture, which should generally apply to the enolic form of many  $\beta$ -diketones.

## ASSOCIATED CONTENT

### Supporting Information

Additional figures and schemes that include kinetic traces at selected wavelengths in pure solvents, comparison of fitting quality, EAS, DAS, SAS, GSB of AA at different excitation wavelength, transient map in the visible region, and linear absorption of AA-Al complex. This material is available free of charge via the Internet at <http://pubs.acs.org>.

## AUTHOR INFORMATION

### Corresponding Author

brixner@phys-chemie.uni-wuerzburg.de

### Present Address

<sup>†</sup>Physikalische Chemie II, Ruhr-Universität Bochum, Universitätsstraße 150, 44780 Bochum, Germany.

### Notes

The authors declare no competing financial interest.

## ACKNOWLEDGMENTS

We thank the German Research Foundation (DFG) for funding within the Research Unit “Light-Induced Dynamics in Molecular Aggregates” (FOR 1809) as well as for support of PN within the Emmy-Noether program and the Cluster of Excellence RESOLV (EXC1069). We are grateful to Dr. Ulrike Selig-Parthey, Michael Förster, and Dr. Martin Kullmann for the contribution to the UV supercontinuum generation. A.S.

thanks the German National Academic Foundation (Studienstiftung des deutschen Volkes) for a scholarship.

## REFERENCES

- (1) Binnemans, K. In *Handbook on the Physics and Chemistry of Rare Earths*; Gschneidner, K. A., Pecharsky, V., Bünzli, J.-C., Eds.; Elsevier: Oxford, 2005; Vol. 35, p 107.
- (2) Shaath, N. A. *Photochem. Photobiol. Sci.* **2010**, *9*, 464.
- (3) Gasparro, F. P.; Mitchnick, M.; Nash, J. F. *Photochem. Photobiol.* **1998**, *68*, 243.
- (4) Cantrell, A.; McGarvey, D. J. *J. Photochem. Photobiol., B* **2001**, *64*, 117.
- (5) Poisson, L.; Roubin, P.; Coussan, S.; Soep, B.; Mestdagh, J.-M. *J. Am. Chem. Soc.* **2008**, *130*, 2974.
- (6) Veierov, D.; Bercovici, T.; Fisher, E.; Mazur, Y.; Yogev, A. *J. Am. Chem. Soc.* **1973**, *95*, 8173.
- (7) Lozada-García, R. R.; Ceponkus, J.; Chevalier, M.; Chin, W.; Mestdagh, J.-M.; Crépin, C. *Phys. Chem. Chem. Phys.* **2012**, *14*, 3450.
- (8) Xu, S.; Park, S. T.; Feenstra, J. S.; Srinivasan, R.; Zewail, A. H. *J. Phys. Chem. A* **2004**, *108*, 6650.
- (9) Veierov, D.; Bercovici, T.; Fischer, E.; Mazur, Y.; Yogev, A. *J. Am. Chem. Soc.* **1977**, *99*, 2723.
- (10) Chiavassa, T.; Verlaque, P.; Pizzala, L.; Allouche, A.; Roubin, P. *J. Phys. Chem.* **1993**, *97*, 5917.
- (11) Coussan, S.; Ferro, Y.; Trivella, A.; Rajzmann, M.; Roubin, P.; Wiczorek, R.; Manca, C.; Piecuch, P.; Kowalski, K.; Wloch, M.; Kucharski, S. A.; Musiał, M. *J. Phys. Chem. A* **2006**, *110*, 3920.
- (12) Tobita, S.; Ohba, J.; Nakagawa, K.; Shizuka, H. *J. Photochem. Photobiol., A* **1995**, *92*, 61.
- (13) Aspée, A.; Aliaga, C.; Scaiano, J. C. *Photochem. Photobiol.* **2007**, *83*, 481.
- (14) Kobayashi, A.; Yamaji, M.; Nakajima, S.; Akiyama, K.; Tero-Kubota, S.; Kato, S.-i.; Nakamura, Y. *Chem. Phys. Lett.* **2013**, *555*, 101.
- (15) Nagashima, N.; Kudoh, S.; Takayanagi, M.; Nakata, M. *J. Phys. Chem. A* **2001**, *105*, 10832.
- (16) Trivella, A.; Wassermann, T. N.; Mestdagh, J. M.; Manca Tanner, C.; Marinelli, F.; Roubin, P.; Coussan, S. *Phys. Chem. Chem. Phys.* **2010**, *12*, 8300.
- (17) Kwon, T.-W.; Watts, B. M. *J. Food Sci.* **1963**, *28*, 627.
- (18) Kwon, T.-W.; Van der Veen, J. J. *J. Agric. Food Chem.* **1968**, *16*, 639.
- (19) Megerle, U.; Pugliesi, I.; Schriever, C.; Sailer, C. F.; Riedle, E. *Appl. Phys. B: Lasers Opt.* **2009**, *96*, 215.
- (20) Pal, S. K.; Mereshchenko, A. S.; El-Khoury, P. Z.; Tarnovsky, A. N. *Chem. Phys. Lett.* **2011**, *507*, 69.
- (21) Thomsen, C. L.; Madsen, D.; Thøgersen, J.; Byberg, J. R.; Keiding, S. R. *J. Chem. Phys.* **1999**, *111*, 703.
- (22) Löwenich, D.; Kleinermanns, K.; Karunakaran, V.; Kovalenko, S. A. *Photochem. Photobiol.* **2008**, *84*, 193.
- (23) Johnson, P. J. M.; Prokhorenko, V. I.; Miller, R. J. D. *Opt. Express* **2009**, *17*, 21488.
- (24) Pullen, S. H.; Anderson, N. A.; Walker, L. A.; Sension, R. J. *J. Chem. Phys.* **1997**, *107*, 4985.
- (25) Riedle, E.; Bradler, M.; Wenninger, M.; Sailer, C. F.; Pugliesi, I. *Faraday Discuss.* **2013**, *163*, 139.
- (26) Schott, S.; Steinbacher, A.; Buback, J.; Nuernberger, P.; Brixner, T. *J. Phys. B: At., Mol. Opt. Phys.* **2014**, *47*, 124014.
- (27) van Stokkum, I. H. M.; Larsen, D. S.; van Grondelle, R. *Biochim. Biophys. Acta, Bioenerg.* **2004**, *1657*, 82.
- (28) Snellenburg, J. J.; Liptenok, S.; Seger, R.; Mullen, K. M.; van Stokkum, I. H. M. *J. Stat. Software* **2012**, *49*, 1.
- (29) Mullen, K. M.; van Stokkum, I. H. M. *J. Stat. Software* **2007**, *18*, 1.
- (30) Snellenburg, J. J.; Dekker, J. P.; van Grondelle, R.; van Stokkum, I. H. M. *J. Phys. Chem. B* **2013**, *117*, 11363.
- (31) Srinivasan, R.; Feenstra, J. S.; Park, S. T.; Xu, S.; Zewail, A. H. *J. Am. Chem. Soc.* **2004**, *126*, 2266.
- (32) Sobolewski, A. L.; Domcke, W. *J. Phys. Chem. A* **1999**, *103*, 4494.
- (33) Upadhyaya, H. P.; Kumar, A.; Naik, P. D. *J. Chem. Phys.* **2003**, *118*, 2590.
- (34) Chen, X.-B.; Fang, W.-H.; Phillips, D. L. *J. Phys. Chem. A* **2006**, *110*, 4434.
- (35) Coe, J. D.; Martínez, T. J. *J. Phys. Chem. A* **2006**, *110*, 618.
- (36) Terranova, Z. L.; Corcelli, S. A. *J. Phys. Chem. Lett.* **2012**, *3*, 1842.
- (37) Lochbrunner, S.; Schultz, T.; Schmitt, M.; Shaffer, J. P.; Zgierski, M. Z.; Stolow, A. *J. Chem. Phys.* **2001**, *114*, 2519.
- (38) Herek, J. L.; Pedersen, S.; Bañares, L.; Zewail, A. H. *J. Chem. Phys.* **1992**, *97*, 9046.
- (39) Arthen-Engeland, T.; Bultmann, T.; Ernsting, N. P.; Rodriguez, M. A.; Thiel, W. *Chem. Phys.* **1992**, *163*, 43.
- (40) Chudoba, C.; Riedle, E.; Pfeiffer, M.; Elsaesser, T. *Chem. Phys. Lett.* **1996**, *263*, 622.
- (41) Yoon, M.-C.; Choi, Y. S.; Kim, S. K. *Chem. Phys. Lett.* **1999**, *300*, 207.
- (42) Trivella, A.; Roubin, P.; Theulé, P.; Rajzmann, M.; Coussan, S.; Manca, C. *J. Phys. Chem. A* **2007**, *111*, 3074.
- (43) Lozada-García, R. R.; Ceponkus, J.; Chin, W.; Chevalier, M.; Crépin, C. *Chem. Phys. Lett.* **2011**, *504*, 142.
- (44) Cordes, T.; Malkmus, S.; DiGirolamo, J. A.; Lees, W. J.; Nenov, A.; Vivie-Riedle, R. d.; Braun, M.; Zinth, W. *J. Phys. Chem. A* **2008**, *112*, 13364.
- (45) Rudolf, P.; Buback, J.; Aulbach, J.; Nuernberger, P.; Brixner, T. *J. Am. Chem. Soc.* **2010**, *132*, 15213.
- (46) Zgrablić, G.; Novello, A. M.; Parmigiani, F. *J. Am. Chem. Soc.* **2011**, *134*, 955.
- (47) Polli, D.; Weingart, O.; Brida, D.; Poli, E.; Maiuri, M.; Spillane, K. M.; Bottoni, A.; Kukura, P.; Mathies, R. A.; Cerullo, G.; Garavelli, M. *Angew. Chem., Int. Ed.* **2014**, *53*, 2504.
- (48) Emsley, J. In *Complex Chemistry*; Springer: Berlin, 1984; p 147.
- (49) Airinei, A.; Homocianu, M.; Dorohoi, D. O. *J. Mol. Liq.* **2010**, *157*, 13.
- (50) Chengbin Jing, X. Z.; Tao, H.; Wang, X.; Liu, A. *J. Mater. Sci. Technol.* **2004**, *20*, 639.
- (51) DiCarlo, E. N.; Watson, E.; Varga, C. E.; Chamberlain, W. J. *J. Phys. Chem.* **1973**, *77*, 1073.
- (52) Bertolasi, V.; Ferretti, V.; Gilli, P.; Yao, X.; Li, C.-J. *New J. Chem.* **2008**, *32*, 694.
- (53) Coultous, C. J. Ph.D. Dissertation, University of Durham, Durham, U.K., 1999.
- (54) Ghosh, R.; Palit, D. K. *Photochem. Photobiol. Sci.* **2013**, *12*, 987.
- (55) Roubin, P.; Chiavassa, T.; Verlaque, P.; Pizzala, L.; Bodot, H. *Chem. Phys. Lett.* **1990**, *175*, 655.
- (56) Ishida, T.; Hirata, F.; Kato, S. *J. Chem. Phys.* **1999**, *110*, 3938.
- (57) Mavri, J.; Grdadolnik, J. *J. Phys. Chem. A* **2001**, *105*, 2045.